

---

# Microsphere and Fiber Optics based Optical Sensors

---

A. Rostami, H. Ahmadi, H. Heidarzadeh and  
A. Taghipour

Additional information is available at the end of the chapter

<http://dx.doi.org/10.5772/57465>

---

## 1. Introduction

Great advantages of optical sensing including immunity to electromagnetic interference, large bandwidth, reliability, and high sensitivity have interested engineers to apply optical sensors instead of electronic sensors for sensing of various environmental parameters. Optical sensors work based on change of intensity, phase, polarization, wavelength and spectral distribution of the light beams by the phenomenon that is being measured. Optical sensors can be used in many areas such as biomedical, civil and aerospace engineering, oil and gas industry, transportation as well as in energy sector. This chapter provides enough information related to optical sensors that is utilized in biomedical engineering especially. First, WGM-based optical biosensors are introduced and studied. Then microsphere resonator is considered as an example and a specific type of WGM-based biosensors. Helmholtz equation is solved for this micro optical-resonator in order to obtain optical modes and Eigen values. Then, capability of microsphere resonator as biosensor is investigated and analyzed based on simulation and comparison to experimental results. Furthermore, fiber optic sensors and their application in biomedical field, specifically in minimally invasive surgeries, are described.

## 2. Optical biosensors based on WGM (Whispering Gallery Mode)

There are different types of biosensors with diverse physical basics such as electrochemical biosensors [1], mass-based biosensors [2], optical biosensors [3], etc., among these different types of biosensors, optical biosensors provide more efficiency because of their exclusive features due to light-based detection. One kind of optical biosensor is whispering gallery mode (WGM)-based biosensor which provides label-free detection [4]. WGM phenomenon occurs in optical microcavities (optical micro resonators) [5]. Optical microcavities confine light in a

circular path and make resonance phenomenon in specific wavelengths [6, 7]. Therefore, the resonance wavelengths emerge as notches in transmission spectrum. There are various types of optical microcavities according to their shapes. Three major types of optical microcavities can be seen in Fig. 1.

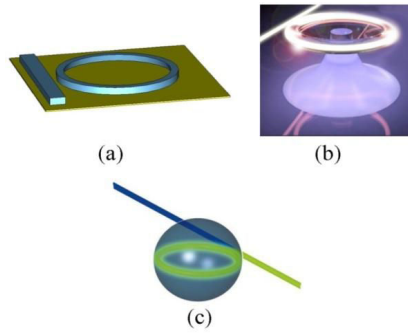


**Figure 1.** Different types of optical microcavities, (a) Micro-ring resonator, (b) Micro-toroid resonator, (c) Micro-sphere resonator.

Despite easy fabrication process, the ring resonator has small quality factor ( $Q$ ) compared to micro toroid and microsphere [5, 6]. Specifically, microspheres are three-dimensional WGM resonators, a few hundred micrometers in diameter, often fabricated by simply melting the tip of an optical fiber. The total optical loss experienced by a WGM in this type of optical micro cavity can be extremely low (quality factor ( $Q$ ) as high as  $10^8$  are routinely demonstrated) [8]. These extraordinary  $Q$ -values translate directly to high energy density, narrow bandwidth for resonant-wavelength and a lengthy path of cavity ring. Because of these advantages, micro-sphere resonators are prone structures for being competent optical biosensors. Fig. 2 shows a microsphere that is coupled to an optical fiber and occurrence of WGM phenomenon.

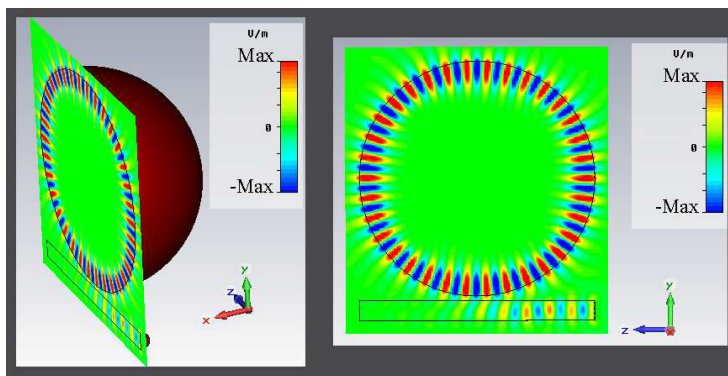


**Figure 2.** WGM phenomenon in microsphere

For analytical description of WGM in microsphere, the Helmholtz equation should be solved in spherical coordinate.

### 2.1. Solution of Helmholtz equation for microsphere optical resonator

In order to theoretically investigate the performance of microsphere, the Maxwell wave equation in microsphere should be solved. For solving the wave equation, the separation of variables technique can be used in order to separate the time variable from spatial variables,

$$u(\vec{r}, t) = \psi(\vec{r})T(t) \quad (1)$$

The part of the solution related to spatial coordinates,  $\psi(\vec{r})$ , satisfies Helmholtz equation as follows.

$$\nabla^2 \psi + k^2 \psi = 0 \quad (2)$$

where  $k^2$  is a separation constant. The Helmholtz equation in spherical coordinates is:

$$\frac{1}{r^2} \frac{\partial}{\partial r} \left( r^2 \frac{\partial \psi}{\partial r} \right) + \frac{1}{r^2 \sin \theta} \frac{\partial}{\partial \theta} \left( \sin \theta \frac{\partial \psi}{\partial \theta} \right) + \frac{1}{r^2 \sin^2 \theta} \frac{\partial^2 \psi}{\partial \phi^2} + k^2 \psi = 0 \quad (3)$$

If we assume that the polarization is constant throughout all space, the separation of variables method can be utilized for solving Helmholtz equation. For applying this method, we consider the solution given by

$$\psi(r, \theta, \phi) = R(r)\Theta(\theta)\Phi(\phi) \quad (4)$$

where  $R(r)$ ,  $\Theta(\theta)$  and  $\Phi(\phi)$  are the radial, polar and azimuthal parts of solution respectively. By applying the considered solution in Helmholtz equation and multiplying by  $\frac{r^2}{R\Theta\Phi}$ , the following equation is obtained:

$$\frac{1}{R} \frac{d}{dr} \left( r^2 \frac{dR}{dr} \right) + k^2 r^2 + \frac{1}{\Theta \sin \theta} \frac{d}{d\theta} \left( \sin \theta \frac{d\Theta}{d\theta} \right) + \frac{1}{\Phi \sin^2 \theta} \frac{d^2 \Phi}{d\phi^2} = 0 \quad (5)$$

Multiplying Eq. (5) by  $\sin^2 \theta$ , the last term should satisfy

$$\frac{1}{\Phi} \frac{d^2 \Phi}{d\phi^2} = -m^2 \quad (6)$$

The solution is

$$\Phi(\phi) = e^{\pm im\phi} \quad (7)$$

where  $m$  is integer because of periodic boundary condition. Inserting Eq. (7) into Eq. (5) the following equation can be obtained.

$$\frac{1}{R} \frac{d}{dr} \left( r^2 \frac{dR}{dr} \right) + k^2 r^2 + \frac{1}{\Theta \sin \theta} \frac{d}{d\theta} \left( \sin \theta \frac{d\Theta}{d\theta} \right) - \frac{m^2}{\sin^2 \theta} = 0 \quad (8)$$

The third and fourth terms in Eq. (8) only depend on  $\theta$ , while the first and second terms only depend on  $r$ . Thus the polar dependence satisfies:

$$\frac{1}{\Theta \sin \theta} \frac{d}{d\theta} \left( \sin \theta \frac{d\Theta}{d\theta} \right) - \frac{m^2}{\sin^2 \theta} = -l(l+1) \quad (9)$$

where the separation constant is considered as  $l(l+1)$  and  $l=0, 1, 2, \dots$ , so that the solution is to be finite at  $\theta=0, \pi$ . With inserting  $x = \cos\theta$ , the equation (9) changes to equation (10) which is Associated Legendre equation.

$$\frac{d}{dx} \left[ (1-x^2) \frac{d\Theta}{dx} \right] + \left( l(l+1) - \frac{m^2}{1-x^2} \right) \Theta(x) = 0 \quad (10)$$

The solution of Eq. (10) is

$$\Theta(x) = P_l^m(x) \quad (x = \cos \theta) \quad (11)$$

where  $P_l^m(\cos\theta)$  are Associated Legendre polynomials and  $|m| \leq l$ .

Usually the polar and azimuthal parts of the solution in Eq. (4) are combined into a spherical harmonic,  $Y_l^m(\theta, \phi)$ , where

$$Y_l^m(\theta, \phi) = C P_l^m(\cos \theta) e^{im\phi} \quad (12)$$

where  $C$  is normalization constant.

From Eq. (8) and (9), the radial dependence in Eq. (4) is given by

$$r^2 \frac{d^2 R}{dr^2} + 2r \frac{dR}{dr} + [k^2 r^2 - l(l+1)] R = 0 \quad (13)$$

Inserting  $Z(r) = R(r)(kr)^{1/2}$  into Eq. (13), we obtain

$$r^2 \frac{d^2 Z}{dr^2} + r \frac{dZ}{dr} + [k^2 r^2 - (l+1/2)^2] Z = 0 \quad (14)$$

which is the Bessel equation of order  $l+1/2$ . The solutions of Eq. (14) are  $J_{l+1/2}(kr)$  and  $N_{l+1/2}(kr)$ . The solutions for  $R(r)$  are the spherical Bessel and Neumann functions,  $j_l(kr)$  and  $n_l(kr)$ , that can be expressed by  $J_{l+1/2}(kr)$  and  $N_{l+1/2}(kr)$  as below:

$$\begin{aligned} j_l(x) &= \sqrt{\frac{\pi}{2x}} J_{l+1/2}(x) & (a) \\ n_l(x) &= \sqrt{\frac{\pi}{2x}} N_{l+1/2}(x) & (b) \end{aligned} \quad (15)$$

Although the mathematical solution for  $R(r)$  consists of Neumann functions, the physical solution does not because the answer is finite in the region of solution. Hence, the general solution of Helmholtz equation in spherical coordinates is

$$\psi(r, \theta, \phi) = \sum_k \sum_{l=0}^{\infty} \sum_{m=-l}^l a_{klm} j_l(kr) Y_l^m(\theta, \phi) \quad (16)$$

where  $a_{klm}$  are determined by boundary conditions.

Solving Helmholtz equation for light in spherical coordinate and using boundary condition across the surface of microsphere, the characteristic equation is obtained as Eq. (17) that describes the relationship between wave vector and eigenvalues  $l$  and  $m$  [9].

$$(\eta_s \alpha_s + 1/R_s) \times j_l(kn_s R_s) = kn_s j_{l+1}(kn_s R_s) \quad (17)$$

where  $\eta_s$  is 1 for TE mode and  $n_s^2/n_0^2$  for TM mode.  $n_s$  and  $n_0$  are refractive indices of sphere and surrounding medium, respectively. Also,  $R_s$  is the radius of microsphere. In Eq. (17),  $\alpha_s = (\beta_l^2 - k^2 n_0^2)^{1/2}$  where  $\beta_l = (l^2 + l)^{1/2} / R_s$ .

## 2.2. Bio-sensor based on microsphere optical resonator

Virus particles are a major cause for human diseases, and their early detection is of great urgency since modern day travel has enabled these diseases agents to be spread through population across the globe [10]. Recently, single-virus detection has been reported based on microsphere resonator, practically [11]. Microsphere resonators are used for biosensing applications on the basis of resonant frequency shift due to attachment of desirable particles to the microsphere surface. There are many cases which microspheres are used as a high sensitive biosensor for detection of particles based on resonance frequency shift [12, 13].

An optical WGM may be represented by a light wave that circumnavigates near the surface of a glass sphere. Attachment of a particle to the surface of microsphere causes shift in resonance frequency of transmission spectrum due to perturbation in path of light [14, 15]. Consequence of this variation in the travelling path of light is satisfaction of condition related to WGM in the other frequency which adverts as shift of resonance frequency. It is obvious from Fig. 2 that in resonance frequency, the light passing in the fiber will be trapped in microsphere, so this frequency will be omitted from transmission spectrum of optical fiber. It is noteworthy to mention that this figure has been obtained from simulation performed by Finite Element Method (FEM). Transmission spectrum of microsphere resonator without particle attachment is shown in Fig. 3. The obtained Q for this microsphere resonator is calculated as  $8.8 \times 10^4$ . This amount of Q is far small from ultimate Q for microsphere which is almost  $10^9$  [16]. This smallness of Q for simulated microsphere is because of small amount of considered diameter. In order to increase the quality factor, size of the microsphere have to be increased, but it decreases capability of single small-size particle detection. So, we have to compromise between these two parameters in practice.

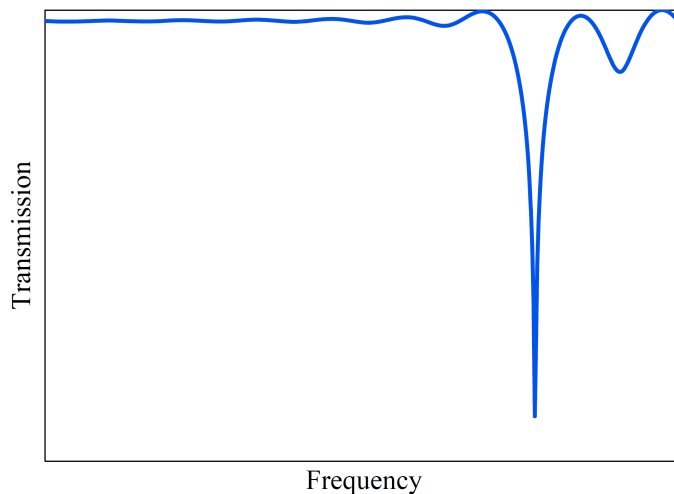


**Figure 3.** Transmission spectrum of microsphere biosensor without particle attachment [17].

Fig. 4 shows the result of attachment a particle to the surface of the microsphere. It causes a shift of resonance notch in the transmission spectrum.

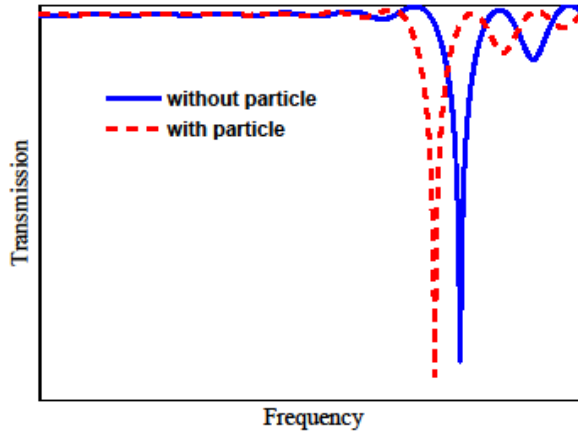


**Figure 4.** Shift of the resonance frequency due to attachment of particle [17].

### 2.2.1. Shift of resonance frequency versus size of attached nanoparticle

Assuming the conserved intensity of resonant light and smallness of the attached particle compared to the wavelength, the frequency of each resonant photon shifts by  $\Delta\omega_r$ , according to [15] and [18].

$$h \Delta\omega_r \cong -\frac{\alpha_{ex}}{2} \langle E^2(r_v, t) \rangle \quad (18)$$

where  $\langle E^2(r_v, t) \rangle$  is the time average of the square electric field at the nanoparticle position ( $r_v$ ). This field is generated due to a single photon resonant state.  $\alpha_{ex}$  is the isotropic excess polarizability including local field effects [11]. By manipulations, the fractional frequency shift is obtained as [15]

$$\frac{\Delta\omega_r}{\omega_r} \cong -\frac{(\alpha_{ex}/\epsilon_0)|E_0(r_v)|^2}{2 \int \epsilon_r(r)|E_0(r)|^2 dV} \quad (19)$$

where  $E_0$  is the electric field amplitude, and  $\epsilon_r(r)$  is the dielectric constant throughout the resonator. The maximum shift for a nanoparticle of radius size  $a_v$  absorbing on the equator is obtained as

$$\left(\frac{\Delta\lambda_r}{\lambda_r}\right)_{\max} \cong D \frac{a_v^3}{R^{5/2} \lambda_r^{1/2}} e^{-a_v/L} \quad (20)$$

where  $L$  is the characteristic length of the evanescent field, and  $D$  is dimensionless dielectric factor associated with both the microsphere and nanoparticle.  $L$  and  $D$  are given by

$$L \approx (\lambda/4\pi)(n_s^2 - n_m^2)^{-1/2} \quad (21)$$

$$D = 2n_m^2 (2n_s)^{1/2} (n_{np}^2 - n_m^2) / (n_s^2 - n_m^2)(n_{np}^2 + 2n_m^2) \quad (22)$$

where  $n_s$ ,  $n_m$  and  $n_{np}$  are the refractive indices of the microsphere, surrounding medium and nanoparticle respectively [11]. The shifts of resonance frequency for three radiuses of particle, 100nm, 150nm, and 200nm have been obtained through FEM simulation. Comparison between simulation results and calculated results extracted from Eq. (20) has been provided in Fig 5. There is good agreement between our simulation results and Eq. (20). The amount of resonance frequency shift increases by enhancement of particle's radius. This fact is reasonable because the path of light through the attached particle increases further when the radius of particle is enhanced. It is noteworthy to mention that the size, shape and refractive index of particles for simulation are selected regarding the characteristics of viruses. Majority of viruses are spherical in shape and their radius size are between 20 to 400 nm [19].

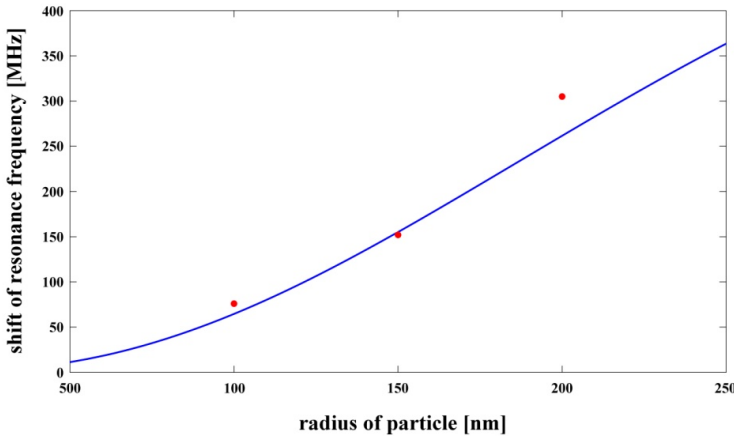
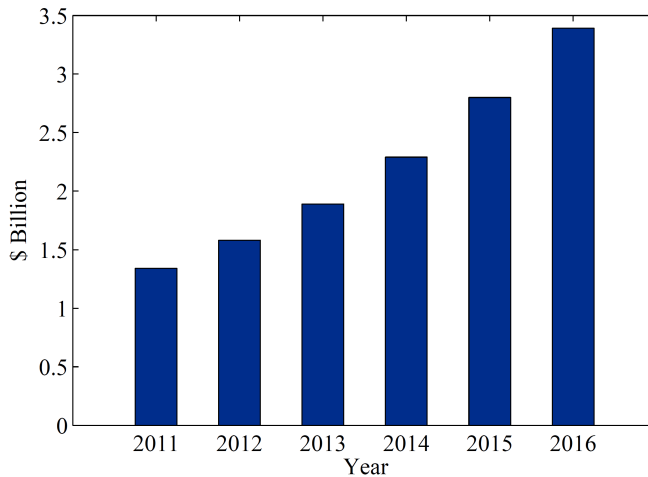


Figure 5. Shift of resonance frequency versus radius of particles [17].

### 3. Fiber optic sensors

One type of optical sensors is fiber optic sensors which have exclusive advantages such as low weight, capability of self-referencing and serial fashion multiplexing. According to market research report, worldwide use of fiber optic sensors will reach \$3.39 billion in 2016 [20]. In the following diagram increasing trend of fiber optic sensors market is shown.



**Figure 6.** Increasing trend of market of fiber optic sensors.

Fiber optic sensors are classified in two categories: extrinsic fiber optic sensors and intrinsic fiber optic sensors. Extrinsic fiber optic sensors are optical fibers that lead up to and out of a “black box” that modulates the light beam passing through it in response to an environmental effect [21]. Intrinsic fiber optic sensors rely on the light beam propagating through the optical fiber being modulated by the environmental effect either directly or through environmentally induced optical path length changes in the fiber itself [21]. In the following, several fiber optic sensors which are utilized for surgeries have been investigated. These fiber optic sensors are intrinsic type.

#### 3.1. Smart surgical instruments based on fiber optic sensors

Nowadays, minimally invasive surgeries are becoming more common as an efficient type of operations in hospitals. By minimally invasive surgeries, surgeon can access to internal body organs of patient through small incisions instead of large openings. During this type of surgeries, surgeons use related specific instruments like clip applicators, laparoscopic graspers, and catheters. Utilizing minimally invasive surgeries decreases recovery time and discomfort for patient. Despite all advantages of minimally invasive surgeries, it has some drawbacks. In open surgery, accuracy of operation is high due to direct visual and touch ability

of the surgeon. On the other hand, in minimally invasive surgery, surgeon loses tactile feedback. Furthermore, navigation of minimally invasive instruments is a challenge in minimally invasive surgeries. Smart minimally invasive surgical instruments have been introduced to overcome such drawbacks. Catheter ablation surgery is a minimally invasive surgery which is performed by surgeon in order to cure cardiac arrhythmias. In this MIS surgery, specific catheters are inserted into inside of heart through main blood vessels of body (Fig. 7, Fig. 8). Then, part of heart which causes cardiac arrhythmias is ablated by ablation catheter [22].

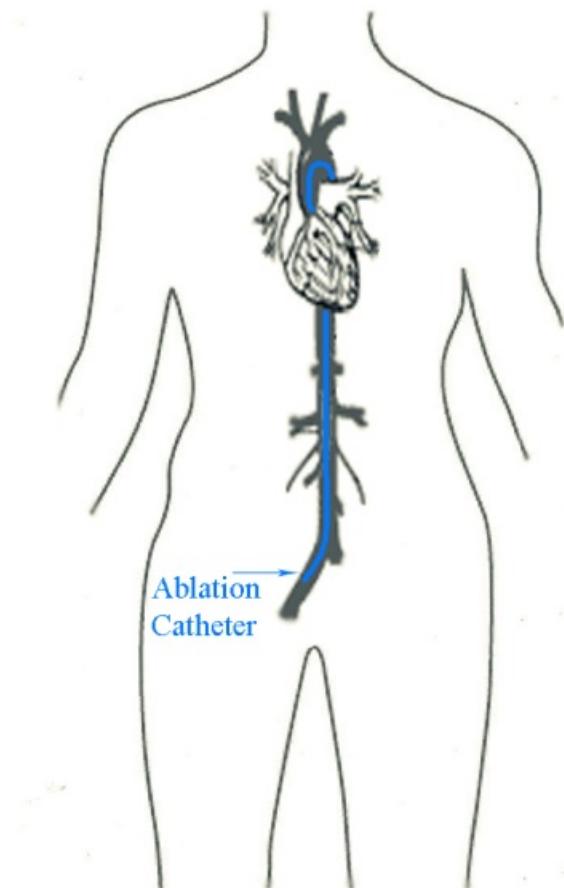


**Figure 7.** Catheter is inserted into inside of heart through Aorta artery.



**Figure 8.** RF ablation catheter.

Outcome of this surgery highly depends on force applied by the ablation catheter's tip to heart tissue. Insufficient force could lead to incomplete ablation, while excessive force may result in serious injury and even perforation [23]. Therefore, to successfully ablate live tissue, the catheter should be applied to the tissue with proper force. Ablation catheters with force sensing capability have emerged recently in order to help surgeons in performing ablation surgery with more accuracy and safety. Many papers and patents have been published in the area of smart ablation catheters. The first introduced generation of smart ablation catheters utilize force sensors in the shaft outside the patient's body [24, 25]. They provide some information of catheter-tip contact forces, but frictional forces due to the interaction between the catheter and blood vessels disturb the measurement, so exact contact force between catheter's tip and heart tissue cannot be measured. Various types of force sensors like capacitive, inductive, resistive and optical sensors can be integrated into the ablation catheter's tip in order to measure contact force, however, fiber optic sensors have been utilized efficiently rather than other types because of their exclusive advantages. TactiCath is one of the smart ablation catheters, provided by Endosense medical technology company that measures the contact force between catheter's tip and heart tissue based on fiber optic sensor [26]. Contact force between catheter's tip and heart tissue can be decomposed into three main axes, one axial force and two lateral forces. Fig. 9 shows the concept of axial and lateral force with respect to catheter's tip.



**Figure 9.** Axial and lateral force with respect to catheter's tip.

Smart ablation catheters that utilize fiber optic sensor as sensing element can be categorized into two main groups based on sensing technology: FBG-based and light intensity modulation based. The basic principle of operation commonly used in a FBG-based sensor is shift of Bragg wavelength. The Bragg wavelength of a FBG ( $\lambda_B$ ) is given by  $\lambda_B = 2n\Lambda$ , where  $n$  is effective index of core and  $\Lambda$  is grating period. Shift of Bragg wavelength ( $\Delta\lambda_B$ ) due to strain ( $\varepsilon$ ) can be expressed by below expression [27] :

$$\Delta\lambda_B = 2n\Lambda \left( 1 - \left( \frac{n^2}{2} \right) (P_{12} - \nu(P_{11} + P_{12})) \right) \varepsilon \quad (23)$$

where  $P_{11}$  and  $P_{12}$  are strain-optic coefficients and  $\nu$  is Poisson's ratio.

FBGs can be used as strain gauges in distal end of the catheter to measure contact force between catheter's tip and heart tissue. Ref. [28] suggests a design which utilizes groups of axially oriented strain gauges (for example FBGs) embedded on distal end of minimally invasive surgical instrument (for instance ablation catheters) to measure forces at the distal end of instrument (Fig. 10). This sensor can measure lateral applied force without temperature sensitivity but temperature variation makes error in axial force measurement for this sensor.

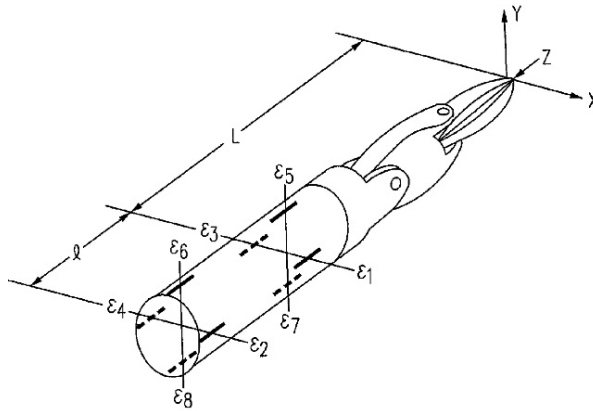


**Figure 10.** A minimally invasive surgical instrument with 8 embedded strain gauge for tri-axial contact force sensing (Reference [28]).

Four optical fibers, that each one has two serial FBGs, can be utilized as embedded strain gauges illustrated in Fig. 10. In such a smart minimally invasive instrument, lateral forces are calculated by  $F_x = (\varepsilon_1 - \varepsilon_2 - \varepsilon_3 + \varepsilon_4)EI / 2lr$  and  $F_y = (\varepsilon_5 - \varepsilon_6 - \varepsilon_7 + \varepsilon_8)EI / 2lr$ . Here,  $E$  is the Young's modulus of material,  $I$  is the section moment of inertia,  $l$  is the distance between two in-line strain gauges, and  $r$  is the radius from  $z$ -axis to the acting plane of the gauges. Axial force is calculated by  $F_z = (\varepsilon_1 + \varepsilon_2 + \varepsilon_3 + \varepsilon_4 + \varepsilon_5 + \varepsilon_6 + \varepsilon_7 + \varepsilon_8)EA / 8$ . Here,  $A$  is cross-sectional area of instrument. Calculated lateral forces ( $F_x$  and  $F_y$ ) are temperature insensitive because of related

differential relation. Light intensity modulation can be used for contact force detection. In this method, distance between a reflector plane and tip of an optical fiber change due to applied force. This change of distance results in change of intensity of reflected light. Fig. 11 shows a smart ablation catheter with contact force sensing capability. Fig. 4 shows details of this catheter. An optical fiber, embedded inside of the catheter, emits light to surface of reflector plane. Intensity of reflected light, which is received by the same optical fiber, depends on distance between optical fiber's tip and reflector plane. When a contact force is applied, the elastic material (which is a polychloroprene rubber) deforms, decreasing the distance between optical fiber's tip and reflector, subsequently, increasing intensity of reflected light. It is noteworthy to mention that a  $2 \times 1$  optical coupler is used in order to separate emitted light from reflected light.



**Figure 11.** Ablation catheter with force sensor (Reference [29]). The outer diameter is 3mm (9Fr in French scale which is used to express size of catheters).

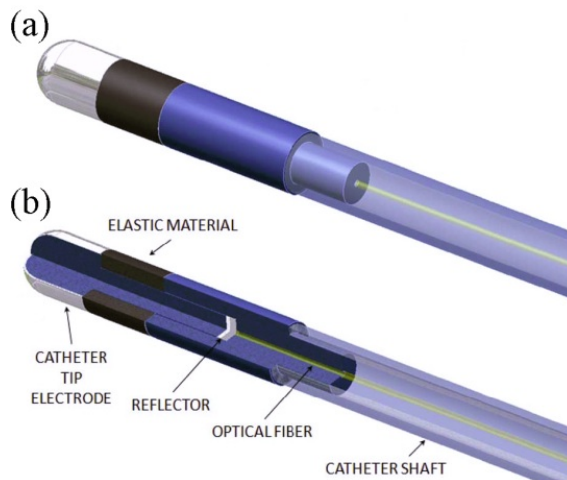


**Figure 12.** (a) Ablation catheter with force sensor. (b) Detailed view of this ablation catheter (Reference [29]).

Components of this sensor were created rapid prototyping technology and are made of photoreactive acrylate polymers. Intensity of reflected light and, consequently, the voltage output produced from an optoelectronic circuit are nonlinear functions of the distance between optical fiber end face and reflector surface [30]. Voltage output that can be detected from an ideal optoelectronic circuit is given by:

$$V = \frac{\pi}{2} \sigma_r k_v w^2 I_0 \left(1 - e^{-\frac{d^2}{2w^2}}\right) \quad (24)$$

In above equation,  $\sigma_r$  is a parameter that represents light losses due to bending and misalignment of optical fiber,  $k_v$  is conversion factor that related light flux to voltage output,  $I_0$  is maximum light intensity of reflected light received by fiber, and  $d$  is diameter of optical fiber. Also, in above equation,  $w$  is defined as  $w = 2 \cdot h \cdot \tan(\gamma) + w_0$ . Here,  $h$  is distance between fiber end surface and reflector surface,  $\gamma$  is divergence angle,  $w_0$  is mode-field radius related to light intensity distribution profile of transmitted light beam. As it can be inferred from equation (24), bending of optical fiber affects voltage output. This is due to bending losses which decrease intensity of transmitted light. During ablation surgery, catheter has several bending, thus an error occurs in contact force measurement due to bending losses. This is a disadvantage of light intensity modulation method of sensing in comparison with FBG method of sensing. Fig. 13 shows voltage output versus applied force to aforementioned catheter's tip.

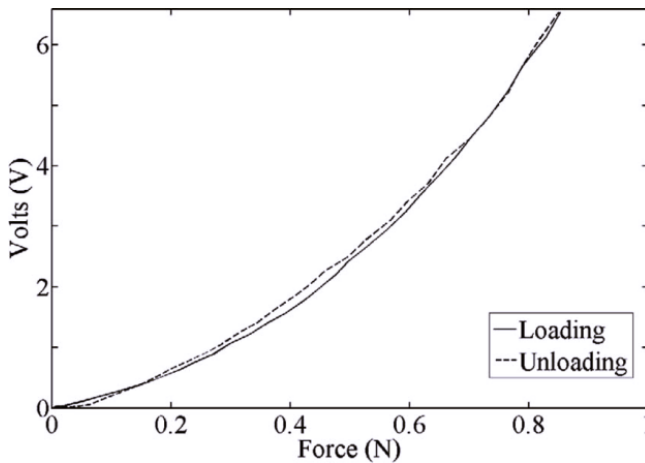
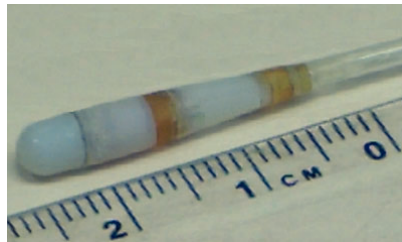


**Figure 13.** Loading and unloading hysteresis cycle of catheter force sensor.

Fig. 13 shows that this force sensor embedded in ablation catheter can operate with very low hysteresis (maximum calculated hysteresis ratio=2.35%). Below quadratic equation can be used to describe nonlinear behavior of force sensor:

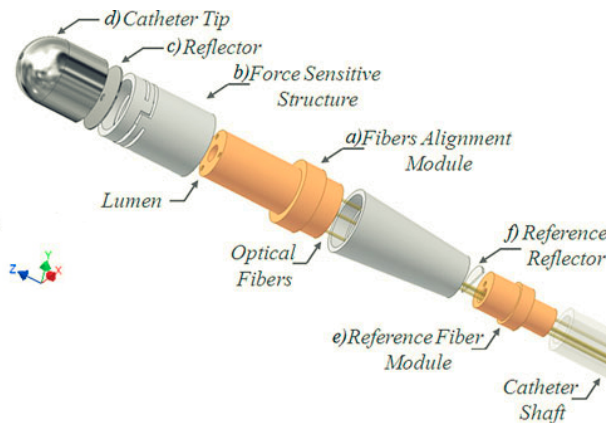
$$V = AF^2 + BF \quad (25)$$

where  $V$  is the voltage output of the force sensor, when a force  $F$  is applied at the catheter tip, and  $A$ ,  $B$  are the calibration coefficients. It is noteworthy to mention that this smart catheter can measure only applied axial forces. For tri-axial contact force sensing, several optical fibers should be utilized. Fig.14 shows a tri-axial ablation catheter force sensor [31]. This sensor is able to measure axial forces of up to 0.50N and lateral forces up to 0.45N with force sensing resolution of 0.01N.



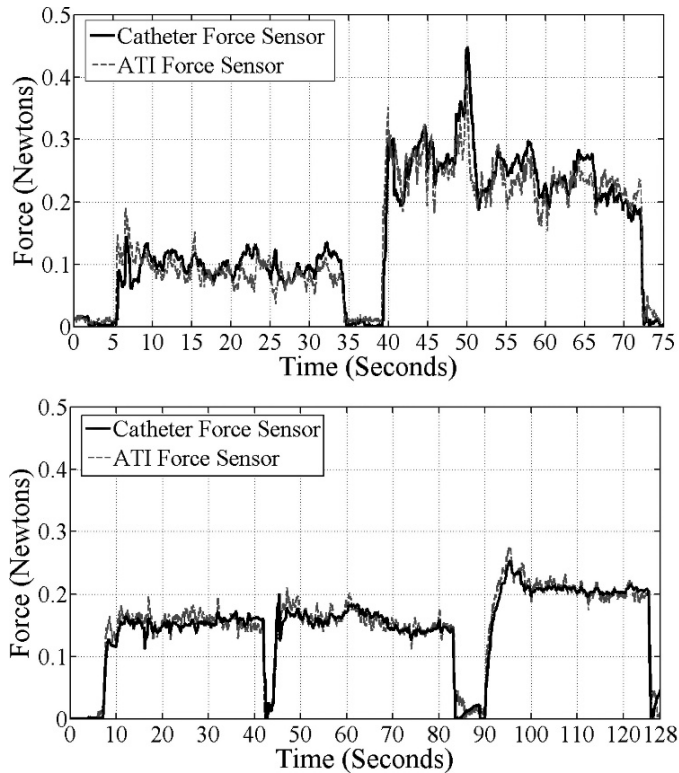
**Figure 14.** Ablation catheter with tri-axial force sensor

Fig.15 depicts detailed view of this smart ablation catheter. This smart catheter has four optical fibers. Three of them are utilized for tri-axial contact force measurement and fourth is reference optical fiber in order to eliminate of bending caused error. The reference optical fiber is always in contact with related reference reflector and, hence, continuously recording the maximum light intensity that can be received by the fibers. Thus, light fluctuations that are not due to contact force between catheter's tip and heart tissue are detectable.



**Figure 15.** Exploded view of ablation catheter with tri-axial force sensor.

High-resolution rapid prototyping technique was employed to create sensing part of this smart catheter using polymeric material. Fig.16 shows comparison results between manufactured smart catheter and standard force sensor (ATI-Nano 17). Both force signals behave similarly with an rms error of 0.03N for the axial case and 0.021N for the lateral case, resulting in a sensor accuracy of 6%.



**Figure 16.** Comparison of the force signals obtained from smart ablation catheter and the standard force sensor, upper panel is related to axial force and lower panel is related to lateral force.

In order to increase the accuracy of minimally invasive surgeries, robotically operation of MIS have been introduced and utilized. The instruments are mounted on robot manipulators controlled by surgeon through joysticks [32-33]. Robots need feedbacks from mounted smart minimally invasive surgeries instruments in order to navigate, control and operate them. Magellan and Sensei-x are examples of robotic catheter systems, manufactured by Hansen Medical [33]. They can also give three dimensional figure of catheters shape inside of patient body. Shape sensing of catheters are based on FBG bending sensors [34].

The amount of bending in a structure is determined by a parameter namely  $K$  and it is defined as:

$$K = \frac{1}{R} \quad (26)$$

The unit of  $K$  is  $[m^{-1}]$ . Bent structure can be supposed on the sector of a circle. In relation (26),  $R$  with unit  $[m]$  is the radius for this imaginary circle. Fig. 17 depicts this matter.

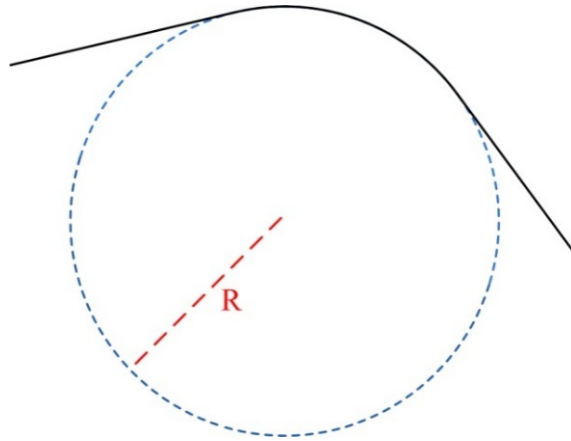


**Figure 17.** A bent structure on the sector of an imaginary circle with radius  $R$

The output of a bent sensor is the amount of structure's bending.

If a catheter get bent around an imaginary circle with radius of  $R$ , like Fig. 18, engendered strain in this fiber is [35] :

$$\varepsilon_z = Kx \quad (27)$$

Engendered strain is extension for  $x > 0$  and compression for  $x < 0$ .

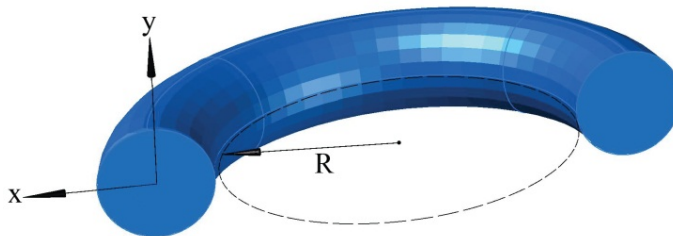


**Figure 18.** Assumed coordinates of fiber and radius of bending

Optical fiber which is placed inside catheter in eccentric position, can measure the amount of bending [36]. Related smart catheters have several optical fibers. These optical fibers have several serial FBGs that measure bending and its direction in different parts of catheter. Assembling obtained shape of bending related to different parts, it is possible to extract the shape of catheter. Three optical fibers can be utilized in order to extract the shape of the catheter [37].

## 4. Summary

Optical sensors are growing fast in all technological fields. This type of sensors is utilized in biomedical engineering, efficiently and according to most roadmaps future is well brilliant for optical sensors in this field of science and technology. Many corporations have been emerged to invest in research, development and fabrication of instruments with optical sensing capability. In this chapter important types of optical sensors including WGM-based sensors and fiber optic sensors, have been investigated with considering their applications in biomedical field.

## Author details

A. Rostami\*, H. Ahmadi, H. Heidarzadeh and A. Taghipour

\*Address all correspondence to: rostami@tabrizu.ac.ir

School of Engineering-Emerging Technologies, University of Tabriz, Tabriz, Iran

## References

- [1] S. Q. Lud, M. G. Nikolaides, I. Haase, M. Fischer and A.R. Bausch, "Field Effect of Screened Charges: Electrical Detection of Peptides and Proteins by a Thin Film Resistor," *Chem. Phys. Chem.* Vol. 7, no. 2, pp. 379-384.
- [2] M. I. R. Gaso, C. M. Iborra, A. M. Baidés, and A. A. Vives, "Surface Generated Acoustic Wave Biosensors for the Detection of Pathogens: A Review," *Sensors*, vol. 9, pp. 5740- 5769, 2009.
- [3] A. M. Armani, R. P. Kulkarni, S. E. Fraser, R. C. Flagan, and K. J. Vahala, "Label-Free, Single-Molecule Detection with Optical Microcavities", *Science*, vol. 317, pp. 783-787, 2007.
- [4] H. Zhu, I. M. White, J. D. Sutter, M. Zourob, and X. Fan, "Miniaturized opto-fluidic ring resonator for sensitive label-free viral detection" *Proc. of SPIE*, vol. 6896, 2008.

- [5] K. J. Vahala, "Optical Microcavities," *Nature*, vol. 424, pp. 839-846, 2003.
- [6] J. P. Laine, *Design and Applications of Optical Microsphere Resonators*, Helsinki University of Technology, Materials Physics Laboratory, 2003.
- [7] L. Collot et al., "Very high-Q whispering-gallery mode resonances observed on fused silica microspheres", *Europhys. Lett.* Vol. 23, pp. 327-334, 1993.
- [8] M. L. Gorodetsky et al., "Optical microsphere resonators: optimal coupling and the ultimate Q," *SPIE*, vol. 3267, pp. 251-262, 1998.
- [9] B. E. Little, J. P. Laine, H. A. Haus, "Analytic Theory of Coupling from Tapered Fibers and Half-Blocks into Microsphere Resonators," *IEEE Journal of Lightwave Technology*, vol. 17, no. 4, pp. 704-715, 1999.
- [10] J. Brockman, *The Next Fifty Years*, New York: Vintage Books, 2002, pp 289-301.
- [11] F. Vollmer, S. Arnold, and D. Keng, "Single Virus Detection from the Reactive Shift of a Whispering-gallery Mode," *PNAS*, vol. 105, no. 52, 2008.
- [12] H. C. Ren, F. Vollmer, S. Arnold, and A. Libchaber, "High-Q microsphere biosensor-analysis for adsorption of rodlike bacteria," *Optics Express*, vol. 15, no. 25, 2007.
- [13] F. Vollmer, and S. Arnold, "Whispering-gallery-mode biosensing: label-free detection down to single molecules," *Nature Methods*, vol. 5, no. 7, 2008.
- [14] F. Vollmer, and S. Arnold, "Whispering-gallery-mode biosensing: label-free detection down to single molecules," *Nature Methods*, vol. 5, no. 7, 2008.
- [15] A. Arnold, M. Khoshshima, and I. Teraoka, "Shift of whispering-gallery modes in microsphere by protein adsorption," *Optics Letters*, vol. 28, no. 4, pp.272-274, 2003.
- [16] M. L. Gorodetsky, A. A. Savchenkov, and V. S. Ilchenko, "Ultimate Q of optical microsphere resonators," *Optics Letters*, vol. 21, no. 7, pp.453-455, 1996
- [17] H. Ahmadi, H. Heidarzadeh, A. Taghipour, A. Rostami, H. Baghban, M. Dolatyari and G. Rostami, *Evaluation of Single Viruse Detection through Optical Biosensor Based on Microsphere Resonator* submitted article to fiber and integrated optics journal
- [18] Arnold S, Ramjit R, Keng D, Kolchenko V, Teraoka I (2008) *Microparticle photophysics illuminates viral biosensing.* *Faraday Discuss* 137:65–85.
- [19] E. Solomon, L. Berg, and D. W. Martin, *Biology*, Stamford, Connecticut: Cengage Learning, 2010, pp.502.
- [20] Market Research Reports, Global Information Inc.
- [21] S. Yin, P. B. Ruffin, and F. T. S. Yu, *Fiber Optic Sensors*, New York: CRC Press, 2008, pp. 2-3.

- [22] S. K. S. Huang, *Catheter Ablation of Cardiac Arrhythmias*, Philadelphia: Elsevier Saunders, 2010.
- [23] L. Di Biase et al., "Relationship between Catheter Forces, Lesion Characteristics, "Popping," and Char Formation: Experience with Robotic Navigation System," *Journal of Cardiovasc. Electrophysiol.* vol. 20, no. 4, pp. 436-440, 2008.
- [24] J. Rosen et al. "Surgeon-Tool Force/Torque Signatures - Evaluation of Surgical Skills in Minimally Invasive Surgery," In *Proc. of Medicine Meets Virtual Reality*, San Francisco, 1999.
- [25] P. Kanagaratnam et al., "Experience of robotic catheter ablation in humans using a novel remotely steerable catheter sheath," *Journal of Interv. Card. Electrophysiol.* Vol. 20, pp. 19-26, 2008.
- [26] Endosense Inc., [www.endosense.com/](http://www.endosense.com/)
- [27] A. D. Kersey et al., "Fiber Grating Sensors," *Journal of Lightwave Technology*, Vol. 15, No. 8, 1997.
- [28] S. J. Blumenkranz, D. Q. Larkin, *Force and Torque Sensing for Surgical Instruments*, US Patent, US20070151390, 2007.
- [29] P. Polygerinos et al., "MRI-Compatible Intensity-Modulated Force Sensor for Cardiac Catheterization Procedure," *IEEE Transaction on Biomedical Engineering*, Vol.58, No. 3, 2011.
- [30] P. Polygerinos, L. D. Seneviratne and K. Althoefer, "Modeling of Light Intensity-Modulated Fiber Optic Displacement Sensors," *IEEE Transaction on Instrumentation and Measurement*, Vol. 60, No. 4, 2011.
- [31] P. Polygerinos et al., "Triaxial Catheter-Tip Force Sensor for MRI-Guided Cardiac Procedures," *IEEE/ASME Transactions on Mechatronics*, Vol. 18, No. 1, 2013.
- [32] Intuitive Surgical Inc., <http://www.intuitivesurgical.com/>
- [33] Hansen Medical Inc., <http://www.hansenmedical.com/>
- [34] M. J. Roelle et al., *Fiber Optic Instrument Sensing System*, US Patent, US201110319815, 2011.
- [35] F. P. Beer, E. R. Johnston and J. T. Dewolf. 2006. *Mechanics of Materials*. Mc Graw Hill.
- [36] A. Rostami et al., "Grating-Based Fiber Bending Sensors with Wide Bending Range," In *Proc. of ISOT'12 Intl. Symposium on Optomechatronic Technologies*, 2012.
- [37] J. P. Moore and M. D. Rogge, "Shape sensing using multi-core fiber optic cable and parametric curve solutions", *Optics Express*, Vol. 20, No. 3, 2012.